

High tolerance detour-phase graphene-oxide flat lens

SHIBIAO WEI,^{1,2} GUIYUAN CAO,^{1,2} HAN LIN,² HAORAN MU,² WENBO LIU,² XIAOCONG YUAN,¹ MICHAEL SOMEKH,¹ AND BAOHUA JIA^{2,3,*}

¹Nanophotonics Research Center, Shenzhen Key Laboratory of Micro-Scale Optical Information Technology, Shenzhen University, Shenzhen 518060, China

²Centre for Translational Atomaterials, Faculty of Engineering, Science and Technology, Swinburne University of Technology, Hawthorn, VIC 3122, Australia

³The Australian Research Council (ARC) Industrial Transformation Training Centre in Surface Engineering for Advanced Materials (SEAM), Swinburne University of Technology, Hawthorn, VIC 3122, Australia

*Corresponding author: bjia@swin.edu.au

Received 24 June 2021; revised 29 September 2021; accepted 21 October 2021; posted 21 October 2021 (Doc. ID 434599); published 16 November 2021

Flat lenses thinner than a wavelength promise to replace conventional refractive lenses in miniaturized optical systems. However, Fresnel zone plate flat lens designs require dense annuli, which significantly challenges nanofabrication resolution. Herein, we propose a new implementation of detour phase graphene flat lens with flexible annular number and width. Several graphene metalenses demonstrated that with a flexible selection of the line density and width, the metalenses can achieve the same focal length without significant distortions. This will significantly weaken the requirement of the nanofabrication system which is important for the development of large-scale flat lenses in industry applications. © 2021 Chinese Laser Press

<https://doi.org/10.1364/PRJ.434599>

1. INTRODUCTION

Optical lenses are indispensable elements in the development of optical systems that have become vital to almost all scientific disciplines [1–3]. With the development of micromachining and nanomachining, portable and wearable high-performance optical devices and systems are now ubiquitous, from mobile phones and smart watches to portable microscopes and spectrometers [4–6]. The miniaturization and integration of optical lenses in these systems require the optical lenses to be ultrathin, flat, and ultralight. However, limited by the mechanism of phase accumulation based on material thickness, conventional refractive lenses are bulky and heavy [7]. Recent breakthroughs in nanophotonics have led to the design and demonstration of a number of ultrathin flat lens concepts, such as the metasurface lens [8–15], super-oscillation lens [16–20], and graphene (and graphene oxide) metalens (GML) [21–26]. These lenses are characterized by their high-resolution, nanometer thickness, ultralight weight, and flat structure, and they can be suitably integrated into all kinds of optical devices and systems. Therefore, ultrathin flat lenses have tremendous potential to replace conventional refractive lenses to realize greater miniaturization and integration of optical devices and systems.

Among the ultrathin flat lenses, the GML has attracted a great deal of attention from scientific to industrial communities because of its unique outstanding properties. Graphene

family materials include graphene, graphene oxide (GO), and reduced graphene oxide. The mechanical robustness and outstanding temperature, chemical, and biological stability of the graphene family materials allow for broad applications not only in daily life, but also in extreme environments [22]. The GML can be fabricated via low-cost and scalable one-step laser nanoprinting techniques [20,27,28]; in contrast, other metalenses require multistep vacuum-based nanofabrication, including electron beam lithography, chemical vapor deposition, and transfer processes [29–30]. These properties make the GML stand out from other ultrathin flat lenses that have been developed to replace conventional refractive lenses in the pursuit of instrument miniaturization and integration, making the study of GML a hot topic. Compared with pure graphene materials, graphene oxide materials have higher transmittance, and have little change in refractive index in a long wavelength range, making it an ideal material for GML [20]. The graphene oxide also can be converted to graphene-like material by using direct laser writing technology, which can fabricate graphene oxide metalenses in a single step [27,28].

At present, the design of GML is based on the Fresnel zone plate, which consists of concentric annular zones. The zones should switch from opaque to transparent or from 0 to π phase values [31–33] at radii $r_n = \sqrt{n\lambda f + n^2\lambda^2/4}$, where n is an integer, λ is the wavelength of the light, and f is the focal length

of the zone plate. However, as the radius of the lens increases, the width of the edge zones becomes narrower, and the density of the zones at the edge is extremely high. The deep subwavelength structures make the fabrication of GML challenging and time-consuming, especially for large-scale lens fabrication; this will limit the range of practical applications based on GML. A new more accurate design concept of GMLs based on the Rayleigh–Sommerfeld theory has been proposed [21], but the ring distributions were similar to that of the Fresnel zone plate, giving the same problem in lens fabrication. Furthermore, it is hard to adjust the design parameters for a fixed focal length because of the rigid relationship between r_n , f , and n . Moreover, as the size of the lens increases, the fabrication accuracy required is higher, and the fabrication tolerance needs to be smaller. For example, a Fresnel-based metalens with a focal length of 300 μm and a diameter of 300 μm has an edge structure with a pitch of about 0.7 μm . In comparison, using the detour phase design method, for the same lens parameters with a focal length of 300 μm and a diameter of 300 μm , the pitch of the structures could be flexibly selected according to the fabrication capability, which has greatly increased the fabrication tolerance. It has to be mentioned that the higher the NA of the lens design, the smaller the features of the edge structure using the Fresnel-based principle, which demands smaller fabrication tolerance. This has greatly limited the range of applicability of Fresnel metalenses.

In this paper, we present high tolerance GML designs based on the detour phase technique. The metalens based on the material of GO is presented, but the design principle is also applicable to other two-dimensional materials. When a lens with the expected focal length is designed with this detour phase method, the parameters such as ring location, ring width, and ring density can be adjusted for convenient design optimization. We designed five GMLs with five different linewidths to demonstrate the high tolerance design requirement of the detour phase method. The experimental results show that lenses designed with different parameters can achieve the same focal length without significant distortions, which greatly relaxes the fabrication requirements. Furthermore, by carefully designing the ring positions, the phase on the focal plane can be precisely modified from 0 to 2π , which may be important for optical systems with high-precision phase control requirements, such as the optical interference system.

2. THEORY OF THE DETOUR PHASE DESIGN

The detour phase technique is a method to modify the complex amplitude distribution of a wavefront by slightly changing the locations of the apertures and the widths of the apertures, which was introduced by Brown and Lohmann in 1966 [34]. This technique has been widely used in computer-generated holography and for applications in beam shaping [35–37], three-dimensional displays, optical signal processing [38], and metasurface device design [39–41]. In this paper, we applied a relatively simple version of the phase detour method, which proved satisfactory for the generation of diffraction-limited focal points. For more complex holograms, however, it may be appropriate to consider other more complex approaches [33,34]. The detour phase technique can be understood by

considering an infinite one-dimensional structure made of periodically repeating apertures, similar to a grating, as shown in Fig. 1(a1). When a light beam passes through two adjacent apertures, it will be diffracted at each aperture and produce secondary wave sources. The first diffraction orders of each secondary wave source form a plane wavefront with parallel ray directions, marked as red arrows. The phase modulation occurs when a spatial shift is introduced to the apertures, which provides an effective method to modify the relative phase value of the first-order diffraction field aperture by aperture. The spatial location shift of the aperture can be defined as the function of the desired phase value:

$$\Delta d = \frac{\Lambda \varphi(x)}{2\pi}, \quad (1)$$

where Λ is the period of the initial grating and $\varphi(x)$ is the desired phase value at point x . This provides a guide for restructuring the wavefront of the diffracted light beam by adjusting the locations of the apertures. For example, for a converging planar lens, a line-structure is designed for shaping the wavefront as an off-axis converging wavefront, as shown in Fig. 1(a2). Then, by rotating the line-structure out of plane along the edge of the line-structure, a converging lens with symmetrical concentric ring structure can be obtained. The light beam undergoes constructive interference to form a symmetrical focal spot.

Figure 1(b) shows the phase distribution along the radial direction of a converging lens. For the discretized paraxial phase profile, different periodicities of the initial grating lead to different aperture locations and thus different lens designs can be obtained. The discretized paraxial phase profile of the converging lens has the following form [42]:

$$\varphi_i(\rho_i, \lambda) = \text{mod}\left(\frac{\pi \rho_i^2}{\lambda f}, 2\pi\right), \quad (2)$$

where ρ_i is the central location of the i th unit to the center of the lens. To form a converging wavefront, the modified locations of the apertures will be

$$\rho'_i = \rho_i + \Delta d_i = \rho_i + \text{mod}\left(\frac{\Lambda \rho_i^2}{2\lambda f}, \Lambda\right). \quad (3)$$

When the desired parameters are selected, the flat lens can be designed following the guidance of Eq. (3). The density of the discretized concentric rings is only dependent on the period of the initial grating Λ . Therefore, lenses with different Λ could be designed with the same focal length, as shown in Fig. 1(c). This will greatly benefit flexible lens design for different application purposes. Furthermore, the aperture could be a transparent region on an opaque material or a π phase aperture on a transparent material, and the linewidth of the aperture could be set to half of the Λ to obtain a high focusing efficiency. Therefore, this design is of high tolerance. Although we used paraxial approximation here, the NA of the lens designed later in the article is about 0.24, which can also work well. For a higher NA lens design, the non-paraxial approximation phase distribution should be used to obtain a more accurate focusing profile.

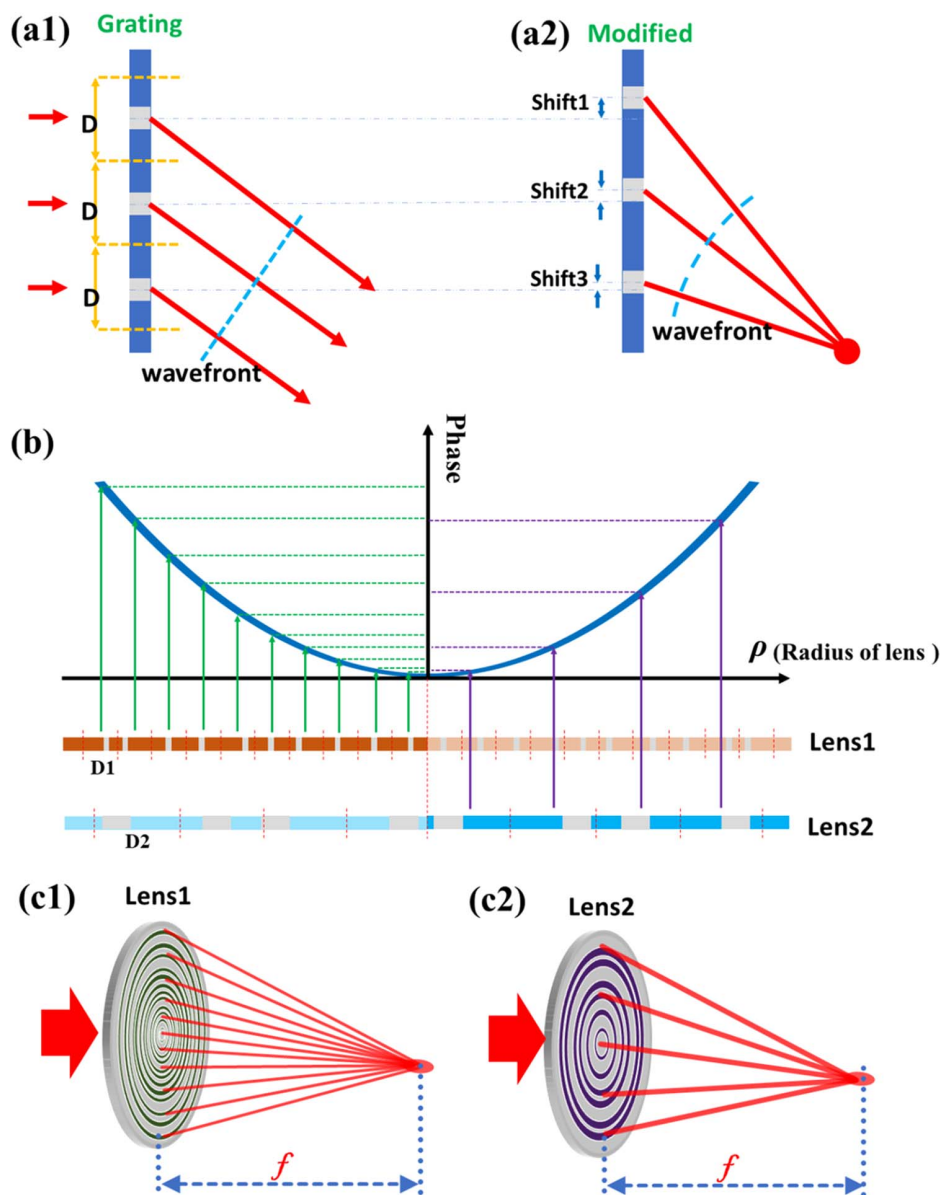


Fig. 1. Flexible lens design based on detour phase holography. (a) The principle of detour phase holography. (a1) Each slit in an infinite one-dimensional grating with periodically repeating apertures of period D acts as a quasi-point-source from which light propagates in all directions. First-order diffraction rays leaving adjacent grating apertures have a path difference of one wavelength; this wavefront is known as a plane wave. (a2) For a converging planar lens, a line-structure is designed to shape the wavefront as an off-axis converging wavefront. (b) Phase distribution along the radial direction of a converging lens. If one aperture of the grating is imperfectly located, the wavefront from the first diffraction order will be deformed. This is undesirable for an ordinary diffraction grating, but it provides a simple way to modify the relative phase value point by point of the first-order diffraction field to form the desired wavefront. (c) Schematic diagram of the flexible lens design. Detour phase holography lenses with the same focal length but different annular parameters (c1) and (c2) could be designed for different applications and fabrication capabilities.

3. EXPERIMENTS AND RESULTS

To prove the effectiveness of the detour phase lens design principle, we designed and fabricated five different lenses based on GO. For all experiments, the working wavelength was 633 nm, the focal length was 300 μm , and the diameter of the lens was 150 μm . To verify the flexibility of our detour phase lens design, the periodicities Λ of the initial gratings were set to be 1–5 μm with a 1 μm step increment. Five GMLs were designed using Eq. (3), with linewidths of 0.5, 1.0, 1.5, 2.0, and 2.5 μm .

The fabrication process includes two steps, as shown in Fig. 2(a): first, coating GO film onto a substrate (cover glass with a refractive index of 1.515); and second, laser patterning of the GML. For the first step, we used the solution-phase layer-by-layer self-assembly method [43], in which the polyelectrolyte polydiallyldimethylammonium chloride (PDDA) and the GO monolayers are coated alternately onto the substrate, leading to a precisely controlled number of layers and film thickness. The thickness of each PDDA–GO bilayer is about 4 nm, so considering the refractive index, a PDDA–GO

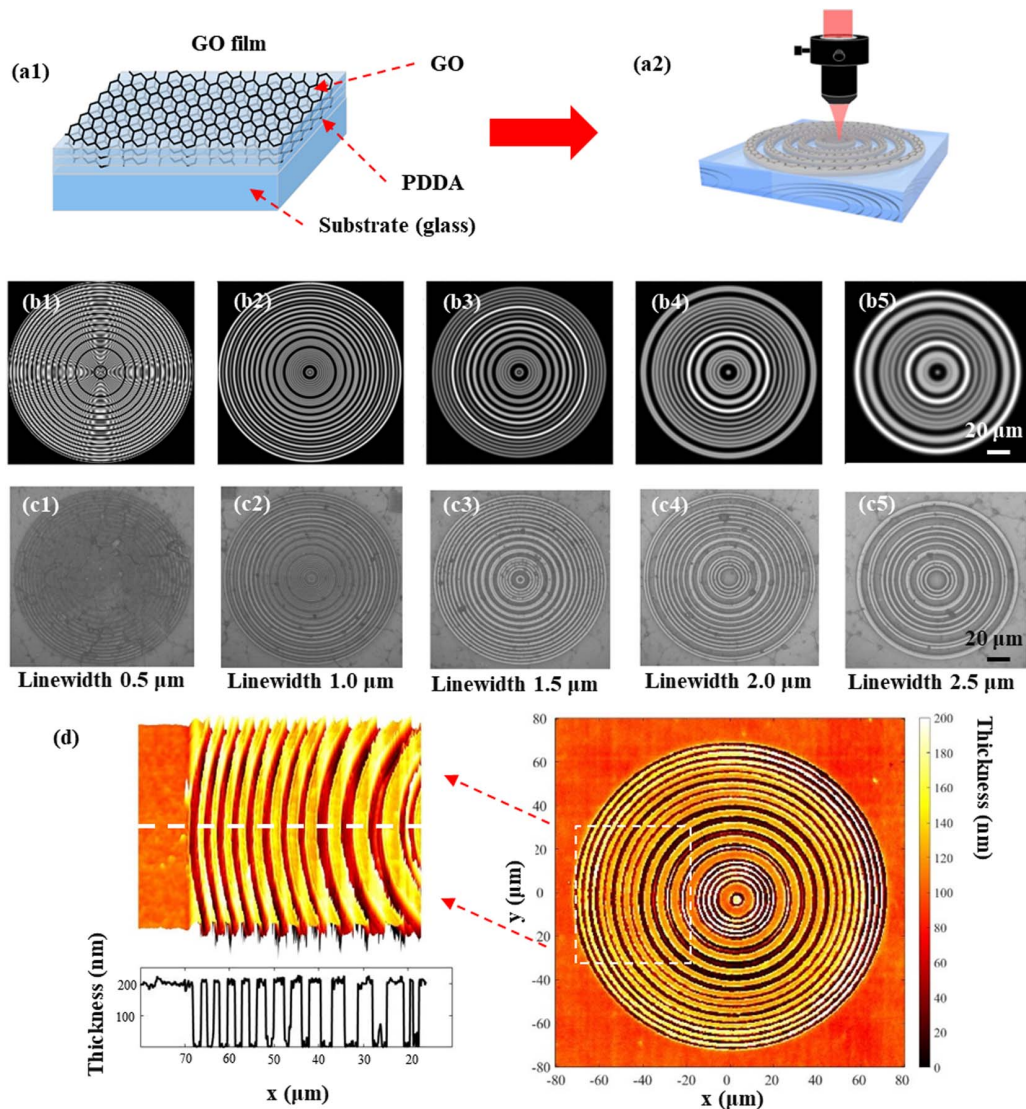


Fig. 2. Flexible GML fabrication. (a) Schematics for GML fabrication: (a1) a GO film was prepared on the glass substrate, followed by (a2) GML patterning of the GO using a mask-free femtosecond laser direct writing system. (b1)–(b5) Different lens designs with the same focal length, but with linewidths of the annular apertures of 0.5, 1.0, 1.5, 2.0, and 2.5 μm; the total number of annular apertures for these lenses is 74, 37, 23, 18, and 13, respectively. (c1)–(c5) The bright-field microscopic images of the fabricated GMLs corresponding to (b1)–(b5). (d) Optical profiler measurements of the GML in (c3), where the thickness of the GML film is 200 nm.

film with 50 bilayers (200 nm thick) was prepared to obtain a π phase delay. Following the coating step, the GML was fabricated using a mask-free femtosecond laser direct writing system (Innofocus Nanoprint3D), with laser ablation creating air apertures on the GO film. Figure 2(b) shows the desired distribution of the concentric air rings (the white part) on the lenses. The linewidths of these five lenses range from 0.5 μm, 1.0 μm, 1.5 μm, 2.0 μm, and 2.5 μm and the lenses had 74, 37, 23, 18, and 13 annular apertures, respectively. The bright-field microscopic images of the fabricated GMLs were obtained by a Nikon microscope (Eclipse Ti2-e) with a 50× objective (NA = 0.55). An optical profiler image in Fig. 2(d) shows greater detail of the GML in Fig. 2(c3). Here, the right inset shows the full GML, with the topography along the white line in the left inset indicating the clearly

defined rectangular shape of the air rings fabricated by laser ablation. The cross section at the bottom of Fig. 2(d) clearly shows the well-defined rings and their thickness.

The schematic of the experimental setup for characterizing the focusing property of the GMLs is shown in Fig. 3. A collimated He–Ne laser with illumination wavelength of 633 nm was used as the incident light source; compared with the size of GMLs, this expanded laser beam was an approximate plane wave. The cross-sectional intensity distribution of the focal spots of the GMLs was captured by an NA = 0.8 objective into a CCD camera. The objective was mounted on a controllable one-dimensional piezo stage. By scanning along the optical axis, the 3D focal intensity distributions of the GMLs were obtained. The x – z intensity distributions of the focal spots are shown in Fig. 4(a) for the lenses

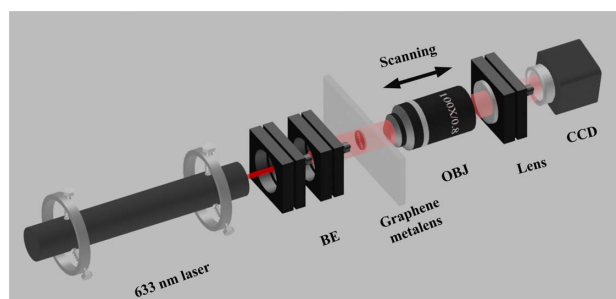


Fig. 3. Schematic of the experimental setup. A 633 nm collimated He–Ne laser was used as the incident light source. A beam expansion (BE) lens group was used to expand the laser beam to obtain an approximate plane wave. An objective (OBJ) with NA = 0.8 was used to collect the beam into a CCD camera. The objective was mounted on a controllable one-dimensional piezo stage. By scanning along the optical axis, the 3D focal intensity distributions of the GMLs were obtained.

with linewidths of 0.5, 1.0, 1.5, 2.0, and 2.5 μm . The corresponding theoretical x – z intensity distributions of the focal spots are shown in Fig. 4(b), which were obtained based on the Rayleigh–Sommerfeld theory [21] programmed in MATLAB. Since this theory does not assume the paraxial approximation, the Rayleigh–Sommerfeld theory gives more accurate predictions. When the linewidths increase, the focusing efficiencies of the GMLs decrease. All intensity values in Fig. 4 are normalized to the peak value. Overall, the experimental measurements match the design very well. The experimental and theoretical focusing intensity distributions along the lateral direction of the designed lenses are shown in Fig. 4(c). The longitudinal intensity distributions along the optical axis for the experimental and theoretical results are shown in Fig. 4(d). The maximum deviation of the focusing position was approximately 5 μm in the longitudinal direction, which is about 1.6% of the focal length ($f = 300 \mu\text{m}$). The mismatch may be caused by two aspects of the measurement method. In the measurement, we must first manually adjust the position of the objective lens to observe the lens and set this position as the initial position ($z = 0 \mu\text{m}$ position). Then, scan along the axial direction to obtain the focusing intensity distributions of the GMLs. Since this process is manually adjusted, errors will inevitably be introduced. The other aspect to affect the accuracy of the experiment result may be caused by the optical measurement by using the objective to image the focal spot to the CCD camera. The measured distributions will be the convolution of the point spread function (PSF) of the lens and the PSF of the objective lens. The measured result will be broadened. The high tolerance of the lens design can be validated, which can greatly benefit practical applications of the flat lens, in particular in complex situations where conventional Fresnel design is incapable of delivering the required performance. Moreover, the high tolerance of the lens design method does not depend on the materials used. Therefore, this research may benefit many research fields, such as the metalens design [8–13] and the design of varifocal lens based on phase-change materials with dynamic control function [44–47]. In the future, the combination of new materials and flexible phase modulation technique will make it possible to

design more practical and easier-to-fabricate dynamic optical devices.

The phase distribution profile of the proposed detour phase lens depends on the shifting distance of the aperture in the periodical structure. Compared with precisely controlling the thickness of the GO to control the desired phase, the shifting distance of the aperture is much easier to achieve with high accuracy positioning stage and no additional processing. We therefore discuss a technique here to precisely control the phase distribution of the focal spots by simply modifying the location of the apertures. The discretized paraxial phase profile of the converging lens should be $\text{mod}(\pi\rho_i^2/\lambda f, 2\pi)$ according to Eq. (2). When an additional uniform phase $\Delta\varphi_c$ is added to the converging phase distribution, $\text{mod}(\pi\rho_i^2/\lambda f + \Delta\varphi_c, 2\pi)$, the phase distribution in the focal spot should be shifted accordingly. By involving an additional uniform phase value to the converging phase distribution of the lens design, the focal length should be unchanged while the phase distribution of the focal spot was shifted. Figures 5(a) and 5(c) show the intensity distributions of two lenses, with one involving a tiny uniform phase shift of 0.1π (about 0.31415 rad) when the lens was designed. The initial period of the lens structure was about 5.2 μm , and therefore, the linewidth of the aperture was about 2.6 μm ; the focal length was set to 500 μm ; and the diameter of the lens was set to 200 μm . Figures 5(b) and 5(d) show the corresponding phase distributions of the two converging lenses. Figures 5(e) and 5(f) show the magnified phase distributions of Figs. 5(b) and 5(d) around the focal spots. Figure 5(g) shows the phase value along the optical axis of Fig. 5(e) (blue line) and Fig. 5(f) (red line). There is a 0.1π phase difference between the two focal spots, which occurred by the aperture position shift in the lens design (about 0.26 μm for Fig. 5). Furthermore, the phase shift value of the focal spot is linear to the additional uniform phase value involved in the lens design, as Fig. 5(h) shows; thus, the accurate control of the phase shift can be realized by the position shift of the aperture. Furthermore, for different periodic structure parameters, the phase sensitivity introduced by the aperture moving the same distance is different. For a given movement precision the phase control improves with increasing period. Taking a design with a period of 4 μm as an example, the sensitivity of phase modification is about 0.436 mm/rad. The technology reported here is a static design. The technology reported here, if combined with new dynamic control mechanism, such as phase-change materials [44–46], may be possible to achieve the accurate control of the dynamic phase. This technique may benefit the metrology industry by requiring a precise phase control of interference fringes, such as structured illumination microscope systems [48,49].

4. CONCLUSION

We have presented a new implementation of flat diffraction lens design using the detour phase hologram principle, which is based on the aperture shift of periodical structures. Compared with the Fresnel zone plate design, this detour phase lens has demonstrated its high tolerance for designing lenses with the same focal length despite possessing different geometrical structures. This will benefit numerous applications for

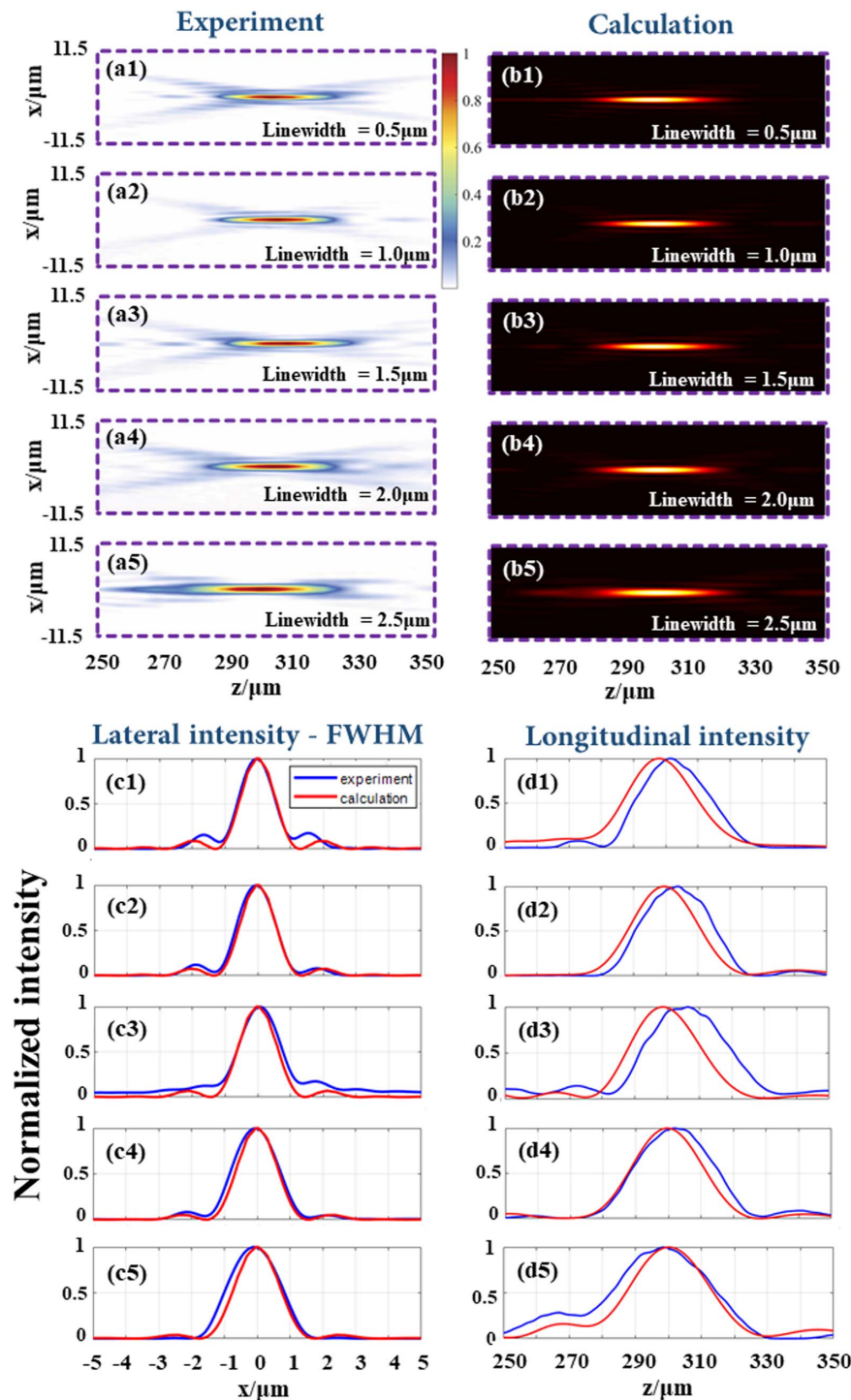


Fig. 4. Experimental characterization. (a1)–(a5) Experimental measurements of longitudinal intensity distribution results of GMLs with different linewidths of the ring-shaped aperture ranging from 0.5 to 2.5 μm . (b1)–(b5) The corresponding theoretical focusing intensity distributions of (a1)–(a5). (c1)–(c5) The experimental and calculated cross-sectional intensity distributions on the focal planes of the five GMLs. (d1)–(d5) The experimental and calculated cross-sectional intensity distributions along the optical axis. The lateral sizes of the focal spot show good agreement between the experimental and theoretical results. The maximal deviation of the focusing position is approximately 5 μm , which is about 1.6% of the focal length (300 μm). All intensity values are normalized to the peak value of intensity.

specializing the design based on specific needs and can significantly relax the fabrication requirements. In the experiment, GMLs were designed and fabricated as examples to verify

the proposed method. Good agreement has been found between the experimental and theoretical results. Furthermore, by considering the uniform phase shift in the lens design,

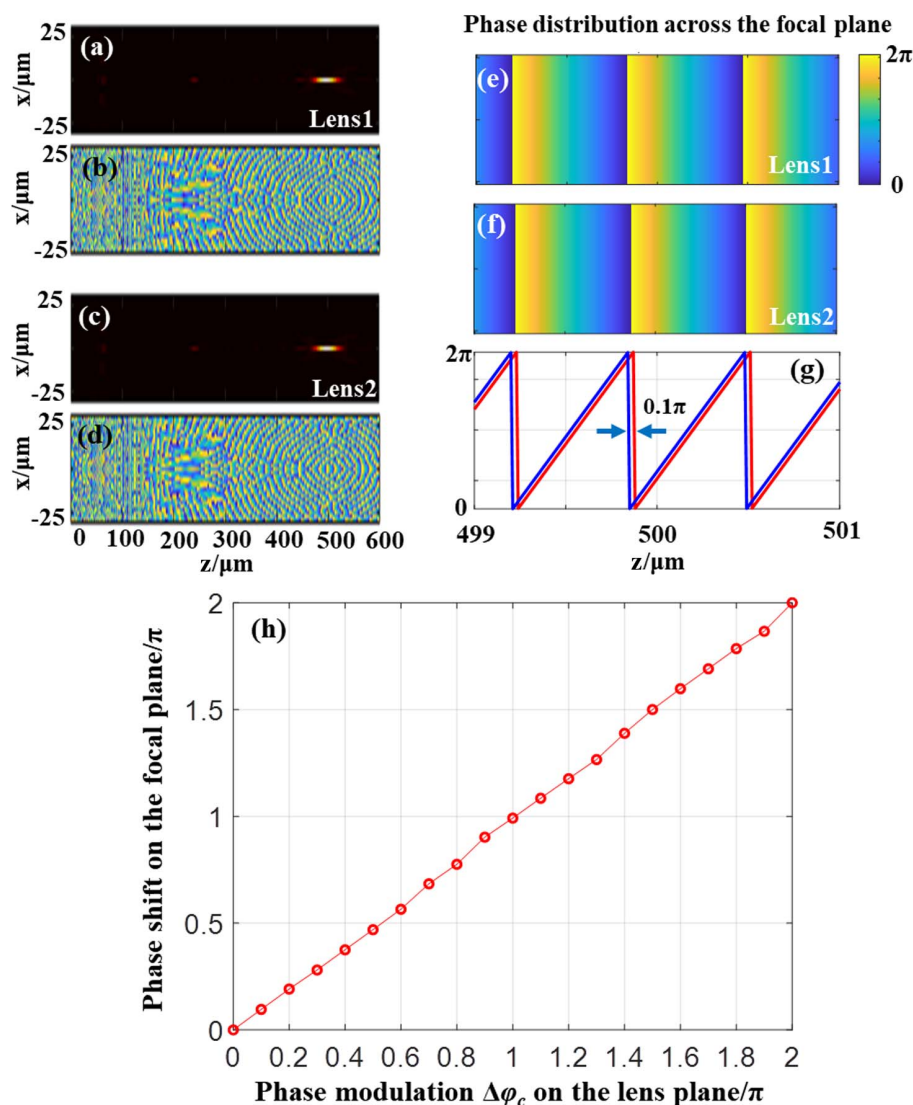


Fig. 5. Phase controlling of the focal spot. (a), (b) The intensity and phase distribution of the focusing field for a GML (lens 1) with the focal length of 500 μm. (c), (d) The intensity and phase distribution of the focusing field for another lens (lens 2), which was obtained by adding a uniform phase value to lens 1. The focal spots of lenses 1 and 2 are the same for the intensity distribution, but the phase distributions crossing the focal plane are slightly modified. (e), (f) The phase distributions of lenses 1 and 2 across the focal plane along the optical axis. (g) The corresponding phase values of (e) (blue) and (f) (red). There is a 0.1π shift of phase value between lenses 1 and 2. (h) The relationship of the additional phase shift of the lens and the phase shift of the focal plane. 0 to 2π phase value shifts of focal spot could be obtained by considering the additional phase shift in the lens design.

the phase distribution of the focal spot could be modified accordingly, with the phase modulation of the focal spot linearly related to the uniform phase shift in the lens design. The detour phase lens design is a promising method that provides optimal high tolerance for a flat diffraction lens design. With less stringent processing requirements, which will reduce the cost of the ultrathin flat lens, this technique will greatly benefit flat lens applications.

APPENDIX A: GO FILM PREPARATION

We used the layer-by-layer process to prepare the GO film. There are five main steps: (1) GO solution is prepared by using a sonifier cell disruptor with 550 W output, 20 kHz frequency

(Branson SFX550); (2) a clean substrate is immersed into a 2.0% (*w/v*) aqueous PDDA (Sigma-Aldrich) solution for 30 s; (3) the substrate is rinsed with de-ionized water and dried with N_2 ; (4) the PDDA-coated substrate is immersed into the prepared GO solution with 0.5 mg/mL concentration for 30 s; (5) the substrate is rinsed again as step (3). One layer of PDDA-GO film is assembled after completing steps (2) to (5). Then by repeating steps (2) to (4), we can construct multilayer GO films.

APPENDIX B: FEMTOSECOND LASER FABRICATION

A low repetition rate, femtosecond pulsed laser beam (100 fs pulse width, 10 kHz, 800 nm) is used to reduce the GO film

through direct laser writing method. By a computer-controlled 3D nanometric piezo stage, 3D arbitrary structures can be created in the sample. The main problem of the GMLs fabrication is to find out the based laser power and speed to ablate the GO film with 0.5 μm linewidth. We used an objective (NA 0.8, 100 \times) to write a series of lines with different laser power and speed, and then measured their profile by atomic force microscope (AFM). The best power (measured before the aperture of the objective) and speed we chose was 12 μW and 30 $\mu\text{m/s}$ to obtain a 0.5 μm linewidth. Based on these parameters, we can fabricate the GMLs with linewidths of 0.5, 1.0, 1.5, 2.0, and 2.5 μm easily.

APPENDIX C: ANALYSIS OF ACCEPTABLE PARAMETER RANGE OF THE STRUCTURE

Here, the focusing efficiency of the lens is used as the selection criterion of the lens design parameters. Essentially, different GML designs for the same focusing spot are the different sampling of the convergent wavefront. Sparse sampling may result in insufficient sampling data and affect the lens's focusing efficiency. As shown in Fig. 6, the focusing efficiencies of GMLs under different linewidths were calculated by finite-difference time-domain (FDTD) method. Both too dense sampling and too sparse sampling will reduce the focusing efficiency of the lens. In this work, we found in a range of linewidths (green area in Fig. 6), the focusing efficiencies of the lenses keep nearly flat. Therefore, the linewidth of the detour phase lens can be appropriately selected according to the processing conditions to achieve the greatest practicality. It is also worth noting that although the focusing efficiency of the lens is reduced to about 8% when the linewidth is 2.5 μm (about 3.95 λ), the quality of

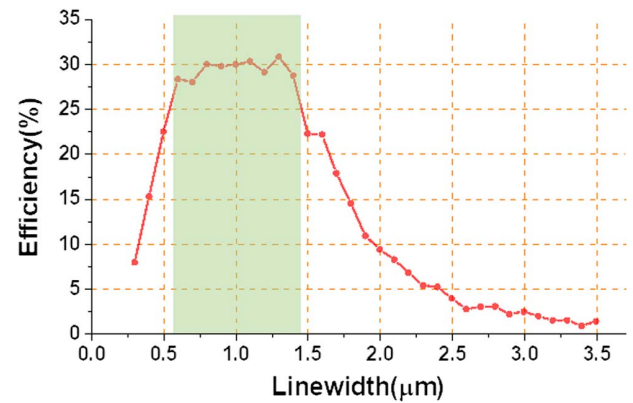


Fig. 6. Focusing efficiencies of GMLs at different linewidths. The focusing efficiency changed when the linewidth of the GO structure changed. Both too dense sampling and too sparse sampling processes of the convergent wavefront will reduce the focusing efficiency of the lens. In the green area, the focusing efficiency of the GMLs did not change significantly.

the focusing spot is still good without obvious distortion, as shown in Fig. 4. This may be meaningful for some applications without the requirement of a high focusing efficiency. For the lens designed in the article, the optimal linewidth range is about 0.55 μm (about 0.869 λ) to 1.45 μm (about 2.29 λ) [the structure period is about 1.1 μm (about 1.74 λ) to 2.9 μm (about 4.58 λ)]. However, the optimal parameters for lens designs with different sizes, numerical apertures, and working wavelengths should be different, which needs to be determined according to the requirements of the individual case.

APPENDIX D: THE TABLE OF RING RADII OF THE GMLS

Lens	Linewidth (μm)	Central Position of the Ring (μm)							
1	0.5	1.10	2.09	3.08	4.06	6.04	7.01	7.97	8.93
		9.89	10.83	11.78	12.72	13.65	14.58	15.50	16.42
		17.32	18.23	19.14	21.04	21.93	22.81	23.69	24.57
		25.44	26.30	27.16	29.02	29.87	30.71	31.55	32.38
		33.21	35.03	35.85	36.66	37.47	38.27	40.07	40.87
		41.65	42.343	43.21	44.98	45.75	46.51	47.27	49.02
		49.76	50.51	51.24	52.97	53.70	54.42	56.14	56.85
		57.55	58.25	59.95	60.64	61.33	63.01	63.68	64.35
		66.02	66.68	67.34	68.99	69.64	70.28	71.91	72.55
		74.17							
2	1	2.70	6.63	8.51	10.35	12.15	13.90	15.61	17.28
		18.91	22.50	24.04	25.54	26.99	30.42	31.79	33.12
		36.42	37.66	38.87	42.04	43.16	46.25	47.29	50.29
		51.25	54.17	55.05	57.89	60.69	61.45	64.17	66.85
		67.48	70.09	72.65	73.16				
3	1.5	2.74	8.47	11.04	13.48	15.77	17.92	22.93	24.79
		29.52	31.11	35.55	36.86	41.02	42.05	45.94	49.69
		53.31	53.78	57.13	60.33	63.41	66.35	69.16	
4	2	8.29	11.61	14.60	17.26	23.58	25.56	31.21	32.53
		37.51	42.18	46.51	50.52	54.20	57.56	60.60	67.33
		69.74							
5	2.5	9.10	12.78	15.81	23.18	24.90	30.97	36.39	41.18
		45.30	53.81	56.68	63.93	65.56			

Funding. Natural Science Foundation of Guangdong Province (2016A030310130); Australia Research Council (the Discovery Project scheme) (DP190103186); Australian Research Council Industrial Transformation Training Centre for Functional Grains (IC180100005); National Natural Science Foundation of China (62175162); Foundation of Shenzhen Science and Technology (20200814100534001); Science, Technology and Innovation Commission of Shenzhen Municipality (KQTD20170330110444030, KQTD20180412181324255); Foundation of Guangdong Education Committee (2020KTSCX117); China Postdoctoral Science Foundation (2021M692173).

Acknowledgment. B. J. acknowledges support from the Australia Research Council and the Industrial Transformation Training Centres. X. Y. acknowledges the Natural Science Foundation of Guangdong Province and the Shenzhen Science and Technology Innovation Commission. S. W. acknowledges the National Natural Science Foundation of China, the Foundation of Guangdong Education Committee, and the Foundation of Shenzhen Science and Technology. S. W. and M. S. acknowledge the Shenzhen Science and Technology Innovation Commission. G. C. acknowledges the fellowship of China Postdoctoral Science Foundation.

S. W., H. L., and B. J. conceived the experiment; S. W. and G. C. performed the experiments and prepared the samples. S. W., X. Y., and M. S. prepared the manuscript. All authors discussed and analyzed the results. B. J. supervised the project.

Disclosures. The authors declare no conflicts of interest.

REFERENCES

- Z. Wang, W. Guo, L. Li, B. Luk'yanchuk, A. Khan, Z. Liu, Z. Chen, and M. Hong, "Optical virtual imaging at 50 nm lateral resolution with a white-light nanoscope," *Nat. Commun.* **2**, 218 (2011).
- D. Liu and Z. Liu, "Hyperlenses and metalenses for far-field super-resolution imaging," *Nat. Commun.* **3**, 1205 (2012).
- S. W. Hell, "Toward fluorescence nanoscopy," *Nat. Biotechnol.* **21**, 1347–1355 (2003).
- A. I. Barbosa, P. Gehlot, K. Sidapra, A. D. Edwards, and N. M. Reis, "Portable smartphone quantitation of prostate specific antigen (PSA) in a fluoropolymer microfluidic device," *Biosens. Bioelectron.* **70**, 5–14 (2015).
- M. M. A. Zeinhom, Y. Wang, Y. Song, M. Zhu, Y. Lin, and D. Du, "A portable smart-phone device for rapid and sensitive detection of *E. coli* O157: H7 in yoghurt and egg," *Biosens. Bioelectron.* **99**, 479–485 (2018).
- K. Karakostas, S. Gkagkanis, K. Katsaliaki, P. Köllensperger, A. Hatzopoulos, and M. E. Kiziroglou, "Portable optical blood scattering sensor," *Microelectron. Eng.* **217**, 111129 (2019).
- R. Kingslake and R. B. Johnson, *Lens Design Fundamentals* (Academic, 2009).
- M. Khorasaninejad, W. T. Chen, R. C. Devlin, J. Oh, A. Y. Zhu, and F. Capasso, "Metalenses at visible wavelengths: diffraction-limited focusing and subwavelength resolution imaging," *Science* **352**, 1190–1194 (2016).
- H. Pahlevaninezhad, M. Khorasaninejad, Y. W. Huang, Z. Shi, L. P. Hariri, D. C. Adams, V. Ding, A. Y. Zhu, C. W. Qiu, and F. Capasso, "Nano-optic endoscope for high-resolution optical coherence tomography *in vivo*," *Nat. Photonics* **12**, 540–547 (2018).
- F. Aieta, P. Genevet, M. A. Kats, N. Yu, R. Blanchard, Z. Gaburro, and F. Capasso, "Aberration-free ultrathin flat lenses and axicons at telecom wavelengths based on plasmonic metasurfaces," *Nano Lett.* **12**, 4932–4936 (2012).
- N. Yu and F. Capasso, "Flat optics with designer metasurfaces," *Nat. Mater.* **13**, 139–150 (2014).
- S. Shrestha, A. C. Overvig, M. Lu, A. Stein, and N. Yu, "Broadband achromatic dielectric metalenses," *Light Sci. Appl.* **7**, 85 (2018).
- B. Xu, H. M. Li, S. L. Gao, X. Hua, C. Yang, C. Chen, F. Yan, S. N. Zhu, and T. Li, "Metalens-integrated compact imaging devices for wide-field microscopy," *Adv. Photonics* **2**, 066004 (2020).
- V. J. Einck, M. Torfeh, A. McClung, D. E. Jung, M. Mansouree, A. Arbabi, and J. J. Watkins, "Scalable nanoimprint lithography process for manufacturing visible metasurfaces composed of high aspect ratio TiO₂ meta-atoms," *ACS Photonics* **8**, 2400–2409 (2021).
- Z. X. Shen, S. H. Zhou, X. N. Li, S. J. Ge, P. Chen, W. Hu, and Y. Q. Lu, "Liquid crystal integrated metalens with tunable chromatic aberration," *Adv. Photonics* **2**, 036002 (2020).
- Y. Aharonov, F. Colombo, I. Sabadini, D. Struppa, and J. Tollaksen, "Some mathematical properties of superoscillations," *J. Phys. A* **44**, 365304 (2011).
- Y. Eliezer, L. Hareli, L. Lobachinsky, S. Froim, and A. Bahabad, "Breaking the temporal resolution limit by superoscillating optical beats," *Phys. Rev. Lett.* **119**, 043903 (2017).
- G. Yuan, E. T. Rogers, and N. I. Zheludev, "Plasmonics" in free space: observation of giant wavevectors, vortices, and energy backflow in superoscillatory optical fields," *Light Sci. Appl.* **8**, 2 (2019).
- Y.-X. Shen, Y.-G. Peng, F. Cai, K. Huang, D.-G. Zhao, C.-W. Qiu, H. Zheng, and X.-F. Zhu, "Ultrasonic super-oscillation wave-packets with an acoustic meta-lens," *Nat. Commun.* **10**, 1 (2019).
- X. Zheng, B. Jia, H. Lin, L. Qiu, D. Li, and M. Gu, "Highly efficient and ultra-broadband graphene oxide ultrathin lenses with three-dimensional subwavelength focusing," *Nat. Commun.* **6**, 8433 (2015).
- G. Cao, X. Gan, H. Lin, and B. Jia, "An accurate design of graphene oxide ultrathin flat lens based on Rayleigh-Sommerfeld theory," *Opto-Electron. Adv.* **1**, 18001201 (2018).
- G. Cao, H. Lin, S. Fraser, X. Zheng, B. Del Rosal, Z. Gan, S. Wei, X. Gan, and B. Jia, "Resilient graphene ultrathin flat lens in aerospace, chemical, and biological harsh environments," *ACS Appl. Mater. Interfaces* **11**, 20298–20303 (2019).
- H. Lin, S. Fraser, M. H. Hong, M. Chhowalla, D. Li, and B. H. Jia, "Near-perfect microlenses based on graphene microbubbles," *Adv. Photonics* **2**, 055001 (2020).
- X. Li, S. Wei, G. Cao, H. Lin, Y. Zhao, and B. Jia, "Graphene metalens for particle nanotracking," *Photonics Res.* **8**, 1316–1322 (2020).
- S. Wei, G. Cao, H. Lin, X. Yuan, M. Somekh, and B. Jia, "A varifocal graphene metalens for broadband zoom imaging covering the entire visible region," *ACS Nano* **15**, 4769–4776 (2021).
- P. Ding, Y. Li, L. Shao, X. Tian, J. Wang, and C. Fan, "Graphene aperture-based metalens for dynamic focusing of terahertz waves," *Opt. Express* **26**, 28038–28050 (2018).
- K.-T. Lin, H. Lin, T. Yang, and B. Jia, "Structured graphene metamaterial selective absorbers for high efficiency and omnidirectional solar thermal energy conversion," *Nat. Commun.* **11**, 1389 (2020).
- H. Lin, B. C. Sturmborg, K.-T. Lin, Y. Yang, X. Zheng, T. K. Chong, C. Martijn de Sterke, and B. Jia, "A 90-nm-thick graphene metamaterial for strong and extremely broadband absorption of unpolarized light," *Nat. Photonics* **13**, 270–276 (2019).
- D. Hu, X. Wang, S. Feng, J. Ye, W. Sun, Q. Kan, P. J. Klar, and Y. Zhang, "Ultrathin terahertz planar elements," *Adv. Opt. Mater.* **1**, 186–191 (2013).
- M. Khorasaninejad, Z. Shi, A. Y. Zhu, W.-T. Chen, V. Sanjeev, A. Zaidi, and F. Capasso, "Achromatic metalens over 60 nm bandwidth in the visible and metalens with reverse chromatic dispersion," *Nano Lett.* **17**, 1819–1824 (2017).
- M. J. Simpson and A. G. Michette, "Imaging properties of modified Fresnel zone plates," *Optica Acta* **31**, 403–413 (1984).
- K. Miyamoto, "The phase Fresnel lens," *J. Opt. Soc. Am.* **51**, 17–20 (1961).
- H. Arsenault, "Diffraction theory of Fresnel zone plates," *J. Opt. Soc. Am.* **58**, 1536 (1968).

34. B. R. Brown and A. W. Lohmann, "Complex spatial filtering with binary masks," *Appl. Opt.* **5**, 967–969 (1966).
35. A. W. Lohmann and D. P. Paris, "Binary Fraunhofer holograms, generated by computer," *Appl. Opt.* **6**, 1739–1748 (1967).
36. B. R. Brown and A. W. Lohmann, "Computer-generated binary holograms," *IBM J. Res. Dev.* **13**, 160–168 (1969).
37. J. P. Hugonin and P. Chavel, "A complement to the theory of Lohmann-type computer holograms," *Opt. Commun.* **16**, 342–346 (1976).
38. T.-C. Poon, *Digital Holography and Three-Dimensional Display: Principles and Applications* (Springer, 2006).
39. C. Min, J. Liu, T. Lei, G. Si, Z. Xie, J. Lin, L. Du, and X. Yuan, "Plasmonic nano-slits assisted polarization selective detour phase meta-hologram," *Laser Photonics Rev.* **10**, 978–985 (2016).
40. J. Lin, P. Genevet, M. A. Kats, N. Antoniou, and F. Capasso, "Nanostructured holograms for broadband manipulation of vector beams," *Nano Lett.* **13**, 4269–4274 (2013).
41. Z. Xie, T. Lei, G. Si, X. Wang, J. Lin, C. Min, and X. Yuan, "Meta-holograms with full parameter control of wavefront over a 1000 nm bandwidth," *ACS Photonics* **4**, 2158–2164 (2017).
42. J. W. Goodman, *Introduction to Fourier Optics* (Roberts and Company, 2005).
43. Y. Yang, H. Lin, B. Zhang, Y. Zhang, X. Zheng, A. Yu, M. Hong, and B. Jia, "Graphene-based multilayered metamaterials with phototunable architecture for on-chip photonic devices," *ACS Photonics* **6**, 1033–1040 (2019).
44. A. Sajjad, O. Hemmatyar, H. Taghinejad, A. Krasnok, Y. Kiarashinejad, M. Zandehshahvar, A. Alù, and A. Adibi, "Tunable nanophotonics enabled by chalcogenide phase-change materials," *Nanophotonics* **9**, 1189–1241 (2020).
45. H. Liu, W. Dong, H. Wang, L. Lu, Q. Ruan, Y. Tan, R. E. Simpson, and J. K. Yang, "Rewritable color nanoprints in antimony trisulfide films," *Sci. Adv.* **6**, eabb7171 (2020).
46. O. Hemmatyar, S. Abdollahramezani, I. Zeimpekis, S. Lepeshov, A. Krasnok, A. I. Khan, K. M. Neilson, C. Teichrib, T. Brown, E. Pop, and D. W. Hewark, "Enhanced meta-displays using advanced phase-change materials," arXiv:2107.12159 (2021).
47. M. Y. Shalaginov, S. An, Y. Zhang, F. Yang, P. Su, V. Liberman, J. B. Chou, C. M. Roberts, M. Kang, C. Rios, and Q. Du, "Reconfigurable all-dielectric metalens with diffraction-limited performance," *Nat. Commun.* **12**, 1225 (2021).
48. M. A. Neil, R. Juškaitis, and T. Wilson, "Method of obtaining optical sectioning by using structured light in a conventional microscope," *Opt. Lett.* **22**, 1905–1907 (1997).
49. K. Wicker, O. Mandula, G. Best, R. Fiolka, and R. Heintzmann, "Phase optimisation for structured illumination microscopy," *Opt. Express* **21**, 2032–2049 (2013).